coatings

MDPI

Article

Sensitivity Analysis of Rotor/Stator Interactions Accounting for Wear and Thermal Effects within Low- and High-Pressure Compressor Stages

Florence Nyssen * and Alain Batailly

Department of Mechanical Engineering, École Polytechnique de Montréal, Montréal, QC H3T 1J4, Canada; alain.batailly@polymtl.ca

* Correspondence: florence.nyssen@polymtl.ca

Received: 20 December 2019; Accepted: 11 January 2020; Published: 15 January 2020

Abstract: In the current design of turbomachines, engine performance is improved by reducing the clearances between the rotating components and the stator, which allows for loss decrease. Due to these clearance reductions, contact events may occur between the rotor and the stator. An abradable coating is deposited along the stator circumference as a sacrificial material to lower the contact severity. However, experiments highlighted the occurrence of rotor/stator interactions with high wear depth on the abradable coating as well as high temperature increases within the abradable coating following contacts. This work focuses on the sensitivity analysis of rotor/stator interactions with respect to the rotor angular speed and the initial clearances between the rotor and the stator, taking into account thermal effects within the abradable coating. Convergence analyses are first conducted to validate the numerical model. Then, after a calibration of the thermal model of the abradable coating based on two experimental test cases, the numerical model is used to investigate the cross effects of the angular speed and the initial clearances on the obtained rotor/stator interactions.

Keywords: turbomachinery; contacts; rotor/stator interactions; abradable coating; thermal effects

1. Introduction

To respect increasingly stringent environmental constraints and to lower operating costs, turbomachine manufacturers are focusing on the improvement of engine performance to decrease fuel consumption [1]. A common solution to lower aerodynamic loss and increase overall performance of an engine consists of the reduction of nominal clearances between rotating bladed disks (rotor) and the surrounding casings (stator). However, this clearance reduction may lead to rotor/stator unilateral contacts and hazardous interaction phenomena [2,3]. In order to reduce the severity of such contact events, an abradable coating is often deposited along the casing contact surface as a sacrificial material [4–6]. A variety of works have been carried out on the numerical simulation of rotor/stator interactions taking into account abradable coating wear [7–9]. Previous work of the authors [10] proposed a numerical strategy to model temperature evolution within the abradable coating following contact events and wear. In this article, this numerical model is improved focusing on two aspects: (1) the definition of the blade heat flux is refined, the latter is now proportional to the friction forces—i.e., therefore also proportional to the contact forces—between the blade and the abradable layer, and (2) a dependence of the mechanical properties of the abradable coating on the temperature is included. In this work, the focus is made on the validation of the contact forces magnitude using two independent experimental data sets. Using the previous definition of the heat flux, an accurate prediction of temperature levels within the structure for two test cases means that contact forces are predicted with a relevant order of magnitude for each configuration.

The first test set-up consists of a rotating high-pressure (HP) compressor's bladed disk, on which the calibration of the numerical model is performed. The focus is made on a 22-lobe torsion interaction, with 22 high temperature areas recorded by an infrared camera localized behind the experimental set-up. The numerical model is calibrated to obtain the same temperature increases than in the experiments. Then, the calibrated model is used to simulate experimental tests carried out on a second experimental test, on a low-pressure (LP) compressor's bladed disk, focusing on a 7-wear-lobe interaction involving the first bending mode. The predicted temperatures using the calibrated model are compared with experimental data of this second test set-up.

The fact that the numerical model—calibrated on the first experiments only—also allows similar temperature increases in the second configuration validates the order of magnitude of the predicted heat flux, and therefore of the predicted contact forces. Based on this conclusion, a detailed sensitivity analysis of the dynamical responses of the system with the clearance between the tip of the blade and the casing is conducted. In particular, the evolution of wear and temperature profiles are analyzed in detail, as well as the effect of the rotor/stator clearances and the angular speed on the observed interactions.

The second section of the article details the numerical model, with a description of each component and of the time integration strategy. Convergence analyses are carried out in the third section with respect to space and time discretization parameters to validate the numerical model. In the fourth section, the calibration of the blade heat flux is performed based on the first considered experimental set-up. Then, the calibrated model is used to simulate the second test case. In the fifth section, an in-depth analysis of the effect of the initial clearance and of the angular speed on the observed rotor/stator interaction is carried out.

2. Numerical Model

The numerical model consists of a single rotating blade and a casing on which an abradable layer is deposited. A detailed description of these three components is presented below, along with the employed time integration algorithm.

2.1. Blade

The blade finite element mesh yields $\mathbf{M}$, $\mathbf{D}$ and $\mathbf{K}(\Omega)$ matrices, respectively the mass, damping and stiffness matrices, with Ω the angular speed. To decrease the size of the model, a modal reduction of the structural matrices is conducted using an existing component mode synthesis method embedding centrifugal effects detailed in [11]. The reduced structural matrices are noted $\mathbf{M}_r$, $\mathbf{D}_r$ and $\mathbf{K}_r(\Omega)$, and the reduction matrix, $\mathbf{\Phi}$, reads:

$$\mathbf{\Phi} = \begin{bmatrix} \mathbf{I} & \mathbf{0} \\ \mathbf{\Phi}_R(0) & \mathbf{\Psi} \end{bmatrix} \tag{1}$$

with:

$$\mathbf{\Psi} = \begin{bmatrix} \mathbf{\Phi}_R\left(\frac{\Omega_{\max}}{2}\right) - \mathbf{\Phi}_R(0) \\ \mathbf{\Phi}_R(\Omega_{\max}) - \mathbf{\Phi}_R(0) \\ \mathbf{\Phi}_L(0) \\ \mathbf{\Phi}_L\left(\frac{\Omega_{\max}}{2}\right) \\ \mathbf{\Phi}_L(\Omega_{\max}) \end{bmatrix}^{\mathsf{T}} \tag{2}$$

in which $\mathbf{\Phi}_R(\Omega)$ and $\mathbf{\Phi}_L(\Omega)$ denote respectively the n_c constraint modes and the first η fixed interface modes computed for a given angular speed Ω. In order to avoid potential rank-deficiency due to similarities between the constraint modes, an orthonormalization of matrix $\mathbf{\Psi}$ is performed. In the

reduced order model, the retained physical degrees of freedom are localized along the blade tip to manage contact interactions. The reduced equation of motion of the blade is given by:

$$\mathbf{M}_r\ddot{\mathbf{q}} + \mathbf{D}_r\dot{\mathbf{q}} + \mathbf{K}_r(\Omega)\,\mathbf{q} + \mathbf{F}^c(\mathbf{q}) = \mathbf{F}^e \tag{3}$$

in which $\mathbf{q}$ contains the reduced degrees of freedom, $\mathbf{F}^c$ denotes the contact forces and $\mathbf{F}^e$ the external forces. An explicit time integration procedure based on the central finite-differences method is used to compute the blade displacement at each iteration $n+1$ as follows [9]:

$$\mathbf{x}^p_{n+1} = \left[\frac{\mathbf{M}}{h^2} + \frac{\mathbf{D}}{2h}\right]^{-1}\left(\left[\frac{2\mathbf{M}}{h^2} - \mathbf{K}\right]\mathbf{x}_n + \left[\frac{\mathbf{D}}{2h} - \frac{\mathbf{M}}{h^2}\right]\mathbf{x}_{n-1}\right) \tag{4}$$

with h the time step of the time integration scheme (referred to as mechanical time step in the following). If blade/abradable coating contacts occur, predicted displacements are corrected using:

$$\mathbf{x}_{n+1} = \mathbf{x}^p_{n+1} + \left[\frac{\mathbf{M}}{h^2} + \frac{\mathbf{D}}{2h}\right]^{-1}\mathbf{F}^c(\mathbf{q}) \tag{5}$$

2.2. Casing

The casing is assumed perfectly rigid, meaning that it remains insensitive to blade contacts. In order to initiate contact, a progressive deformation is applied on the casing at the beginning of the simulation until it reaches a deformed configuration with two lobes, i.e., two privileged contact areas, as illustrated in Figure 1. This two-lobes deformation aims to model the casing ovalization resulting from a thermal imbalance within the engine at rest due to the up motion of the hot gas [12].

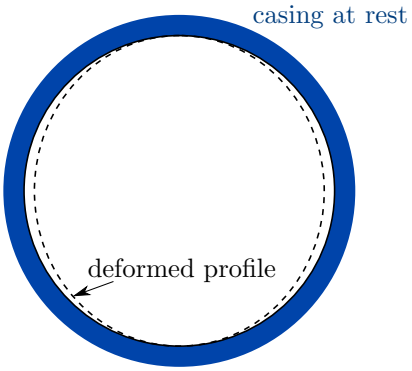

Figure 1. 2-lobe casing deformation.

2.3. Abradable Coating

The abradable coating model is composed of two distinct meshes: (1) a mechanical mesh composed of one-dimensional rod elements to compute wear, and (2) a two-dimensional cylindrical thermal mesh for temperature computation. A weak thermo-mechanical coupling is assumed: thermic influences the system mechanics, but the mechanical deformation of the abradable layer elements has no effect on the computed temperatures. The assumption of weak thermo-mechanical coupling is relevant in the context of rapid dynamics using small time steps and an explicit resolution scheme [13]. It conveniently allows separate solving of the mechanical and the thermal problem. Only heat transfer by conduction is considered.

2.3.1. Mechanical Mesh

The mechanical mesh of the abradable layer consists of one-dimensional two-node rod elements mechanically independent of their neighbors, governed by a plastic constitutive law detailed in [9]. Contact forces resulting from blade/abradable layer contact events cause an elastic deformation of the

rod elements as well as permanent plastic deformations which represents numerically the abradable layer's wear, as illustrated in Figure 2. The evolution of the wear profile of the abradable layer can therefore be computed at each time iteration using this mechanical mesh.

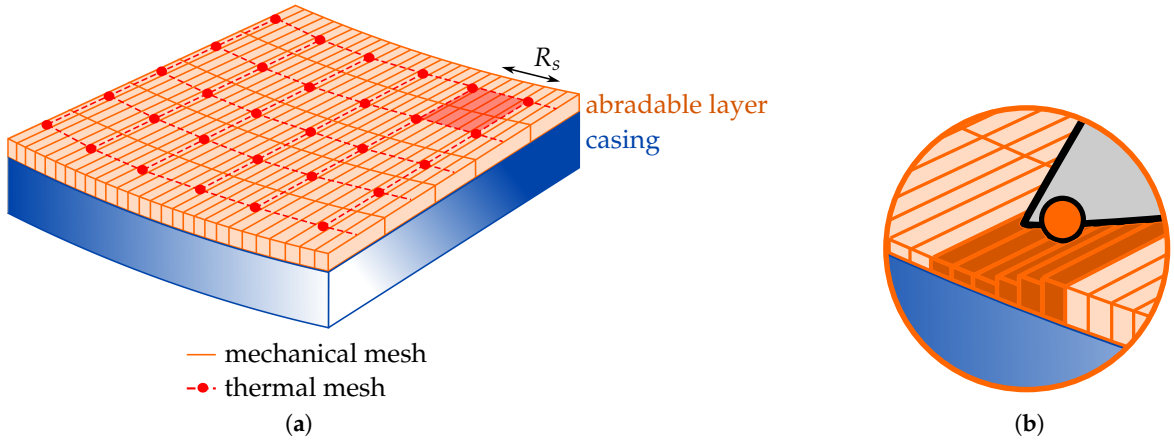

Figure 2. Abradable coating wear mechanism following blade/abradable coating contact event (**a**) and zoom on the abradable layer's wear (**b**).

2.3.2. Thermal Mesh

To compute the temperature evolution within the abradable layer following contact events, a second mesh is added. The latter consists of a two-dimensional thermal mesh superimposed to the mechanical one, as illustrated in Figure 3, with one degree of freedom per node, the nodal temperatures. Along the circumferential direction, one thermal element is considered every R_s mechanical elements, and a contact on any of the R_s mechanical elements will provide a heat flux for the corresponding thermal element, see Figure 3.

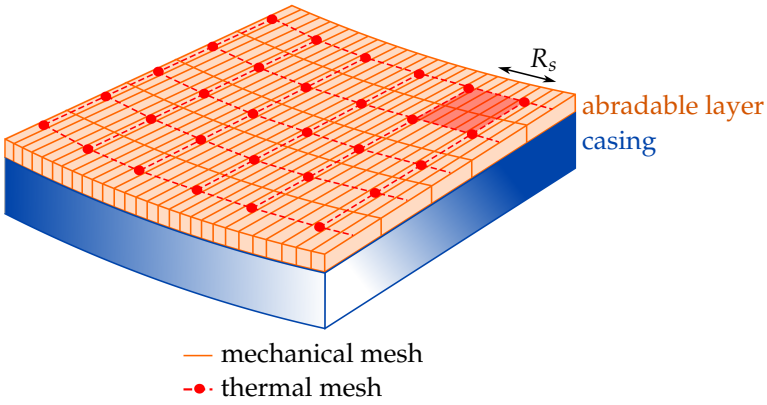

Figure 3. Superimposed mechanical and thermal meshes.

The heat equation, solved on the thermal mesh, is given by [14]:

$$\mathbf{C}_T\dot{\mathbf{T}} + \mathbf{K}_T\mathbf{T} = \mathbf{F}_T \tag{6}$$

in which $\mathbf{T}$ contains the nodal temperatures, $\mathbf{C}_T$ denotes the thermal capacity matrix, $\mathbf{K}_T$ is the thermal conductibility matrix, and the nodal heat flux vector $\mathbf{F}_T$. Thermics and mechanics have different time scales: while the explicit time integration scheme typically requires a time step of 10^{-7} s, thermal problems can be solved with time steps as large as 1 s. Therefore, this equation and the blade equation of motion (Equation (3)) are solved using different time discretizations: the heat equation is

solved every R_t mechanical time steps. The use of these two different space discretization significantly lowers computation times.

The heat flux $\mathbf{F}_T$ in Equation (6) is assumed proportional to the friction forces between the abradable coating and the blade, or if all the abradable coating is removed, between the casing and the blade. At each thermal iteration, the sum of the heat flux generated during the R_t last mechanical time steps is considered, such as:

$$\mathbf{F}_T = \sum_{R_t} q_T \mu \mathbf{t}_n \|\mathbf{v}_t\| \tag{7}$$

in which μ is the friction coefficient (between the abradable coating and the blade or between the casing and the blade depending of the contact components), $\mu\mathbf{t}_n$ the friction forces, $\mathbf{v}_t$ the relative tangential abradable layer/blade velocity (which is approximated here by the blade angular speed Ω) and q_T is a coefficient that will be calibrated in the following using experimental results.

The heat equation (Equation (6)) is solved at each thermal time step, i.e., every R_t mechanical time steps. The evolution of the temperature within the abradable layer is computed at each thermal iteration $t+1$ by solving the system of equations [14]:

$$\mathbf{T}(t+1) = \mathbf{T}(t) + \bar{\mathbf{K}}_T^{-1} \bar{\mathbf{F}}_T(t) \tag{8}$$

with:

$$\begin{aligned} \bar{\mathbf{K}}_T &= \mathbf{C}_T + \alpha' \, \Delta t \, \mathbf{K}_T \\ \bar{\mathbf{F}}_T(t) &= \Delta t \, (\mathbf{F}_T(t) - \mathbf{K}_T \mathbf{T}(s)) \end{aligned} \tag{9}$$

where α' is the integration scheme parameter and $\Delta t = R_t h$ is the thermal time step. One can demonstrate [14] that, in a linear framework, the integration scheme is stable if $\Delta t < \frac{2}{(1-2\alpha')\omega_{max}}$, unconditionally stable for $\alpha' \geq \frac{1}{2}$, and stable without oscillation for $\Delta t < \frac{2}{(1-\alpha')\omega_{max}}$, where ω_{max} denotes the largest eigenfrequency of $\mathbf{C}_T^{-1}\mathbf{K}_T$. In this work, the value of α' is set to $\frac{1}{2}$ such that the scheme is unconditionally stable.

2.3.3. Thermo-Mechanical Coupling

Thermal and mechanical problems are coupled according to two aspects: (1) the thermal expansion of the abradable layer, and (2) the modification of its material properties with temperature. Based on the temperature computed using the thermal mesh, the thermal expansion of each mechanical abradable layer's element at a given iteration t is computed as followed, assuming a linear thermo-elastic constitutive law:

$$\varepsilon_T(t) = \alpha_T \, (\mathbf{T}(t) - \mathbf{T}(t-1)) \tag{10}$$

with ε_T the thermal deformation and α_T the thermal expansion coefficient. For the dependence of material properties with temperature, a linear variation of the Young's modulus E and plastic modulus K of the abradable coating with temperature is assumed in the model. This law can be used as first approximation for aluminum-silicium alloys [15].

2.4. Summary

The blade model, the casing model and the mechanical mesh of the abradable layer are modeled using an existing strategy detailed in [9]. A thermal mesh of the abradable layer is added here to compute temperature increases following contact events. In order to compute temperature elevations within the abradable layer, the heat flux provided by the blade to the abradable layer is assumed proportional to the friction forces between these two components. Two discretization parameters—the spatial and time discretization parameters, denoted R_s and R_t respectively—are involved in the thermal model.

3. Convergence Analysis

In this section, the convergence of the results with respect to both space and time discretization parameters, R_s and R_t respectively, is analyzed. More particularly, the convergence is presented in terms of the abradable layer's wear and temperature profiles at both the leading (LE) and the trailing edges (TE) as well as in terms of blade stresses. Simulations are carried out using the high-pressure (HP) compressor blade's finite element model shown in Figure 4a, and the retained nodes in the reduced order model are marked as red dots.

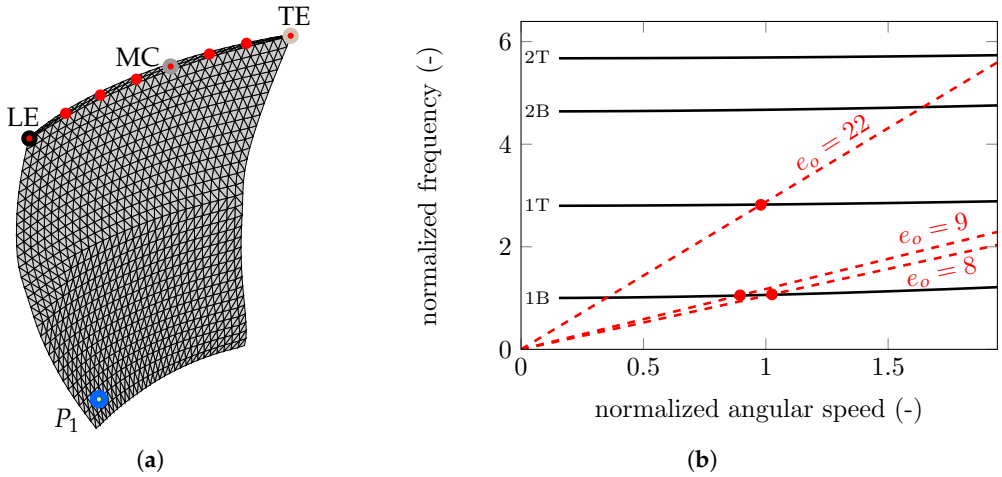

(**a**) (**b**)

Figure 4. Finite element model (**a**) and Campbell diagram (**b**) of the HP compressor blade.

The simulations are run over 100 blade revolutions, at constant angular speed. The chosen angular speed, denoted $\Omega_{\text{exp}}^{\text{HP}}$, corresponds to the excitation of the first torsion (1T) mode with the 22nd engine order (e_o), see the Campbell diagram in Figure 4b [3]. In particular, the selected angular speed is slightly higher than the one corresponding to the curve's intersection because of contact stiffening. The angular speed axis in Figure 4b is normalized using $\Omega_{\text{exp}}^{\text{HP}}$ as reference. The contact is initiated by a 2-lobe casing deformation (see Figure 1). For all simulations, 20,000 mechanical abradable layer elements are considered along the circumferential direction, which ensures that convergence has been reached. The mechanical time step is fixed to h of 10^{-7} s for all simulations. The used value for the friction coefficient μ is 0.1.

Convergence of wear and temperature profiles at both leading and trailing edges at the end of the simulation is shown in Figures 5 and 6, respectively in terms of space and time discretizations. Results show an accurate description of wear and temperature profiles within the abradable layer for $R_s > 100$ (see Figure 5). Small differences appear in temperature profiles for the lowest R_s values, which correspond to a coarser thermal mesh (see the curve referring to $R_s = 100$ in Figure 5c,d).

However, results obtained for all R_t values are perfectly superimposed (see Figure 6). This is due to the different time scales between mechanical and thermal phenomena: considering $R_t = 5000$ leads to a thermal time step of $\Delta t = R_t h = 5000 \times 10^{-7} = 5 \times 10^{-4}$ s, which remains much lower than typical thermal time scales. Simulations with $R_t = 5000$ leads therefore an accurate solution of the heat equation.

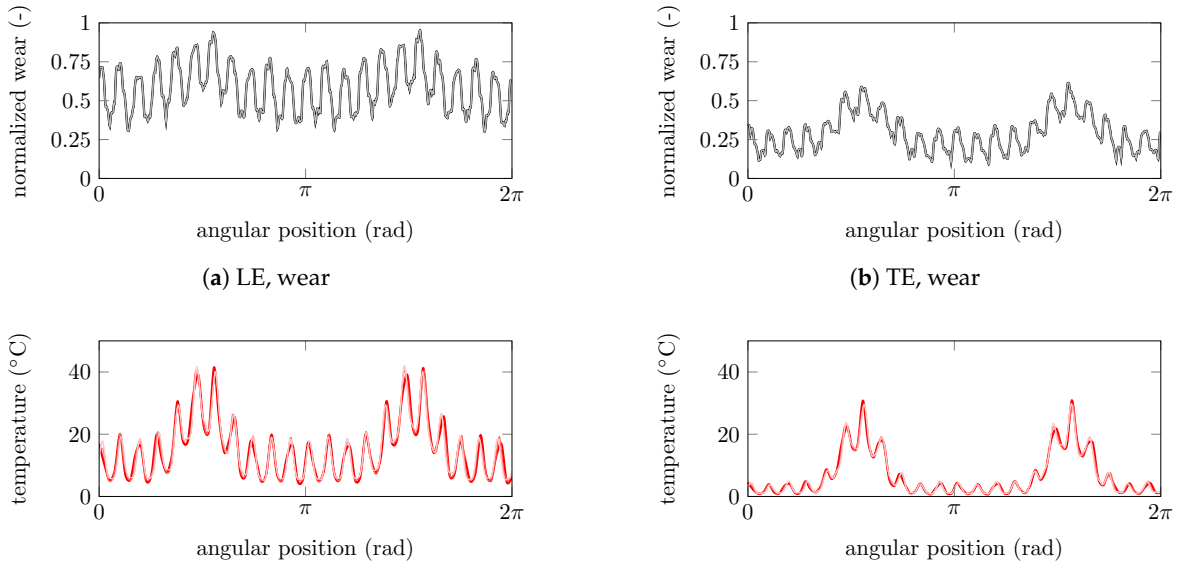

(**a**) LE, wear (**b**) TE, wear

(**c**) LE, temperature (**d**) TE, temperature

Figure 5. Convergence analysis of the wear and temperature profiles at the end of the simulation at the leading and trailing edge with the number of thermal abradable coating elements $n_{ab,th}$: $n_{ab,th} = 80$ or $R_s = 250$ (——/——), $n_{ab,th} = 100$ or $R_s = 200$ (——/——), $n_{ab,th} = 200$ or $R_s = 100$ (——/——), $n_{ab,th} = 250$ or $R_s = 80$ (——/——).

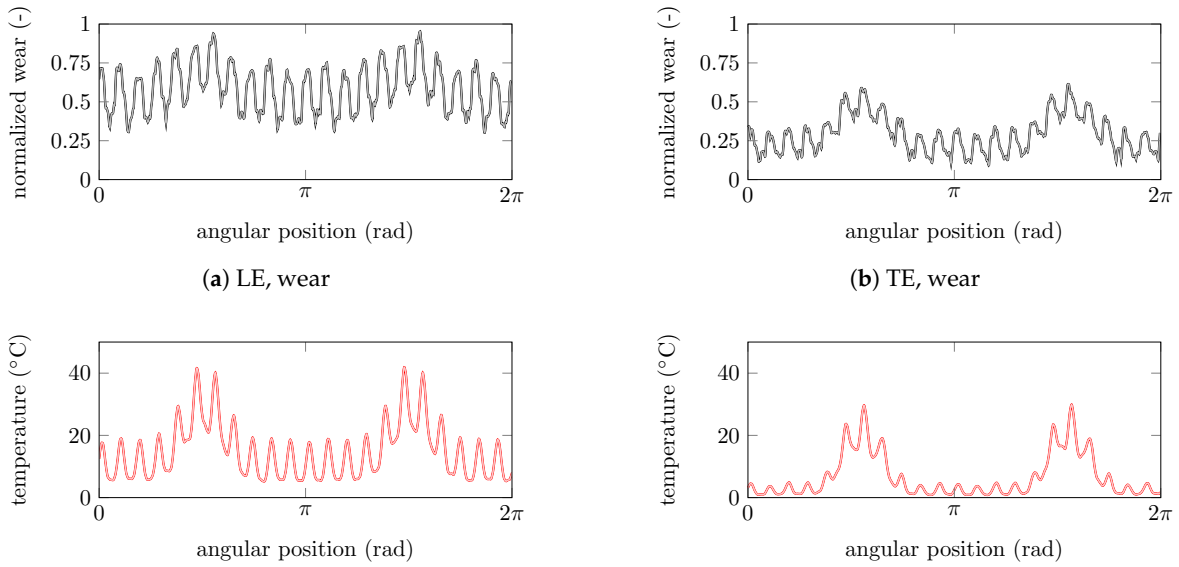

(**a**) LE, wear (**b**) TE, wear

(**c**) LE, temperature (**d**) TE, temperature

Figure 6. Convergence analysis of the wear and temperature profiles at the end of the simulation at the leading and trailing edge with R_t: $R_t = 1$ (——/——), $R_t = 500$ (——/——), $R_t = 1000$ (——/——), $R_t = 5000$ (——/——).

Convergence of blade related quantities is verified in terms of stresses at node P_1, shown in blue in Figure 4a, close to the blade root. This quantity is indeed very sensitive since it relies on predicted blade dynamics and abradable profile evolution. Figure 7 shows the time evolution of the blade stress at node P_1 for several R_s and R_t values. Stresses are computed at the initiation of the interaction. Curves are perfectly superimposed for all R_s and R_t values. This perfect superimposition comes from

the superimposition of the abradable wear profile—the latter indeed directly influences the blade dynamics—for all R_s and R_t values (see Figures 5a,b and 6a,b).

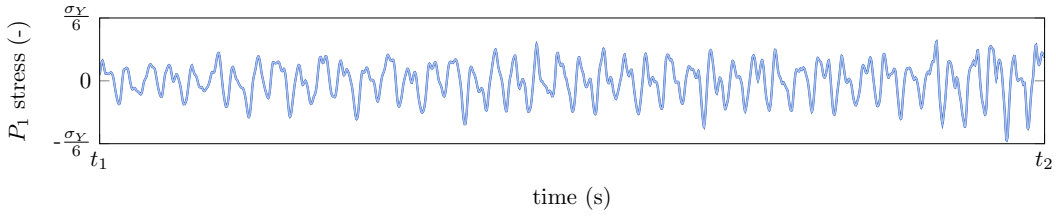

(**a**) space convergence

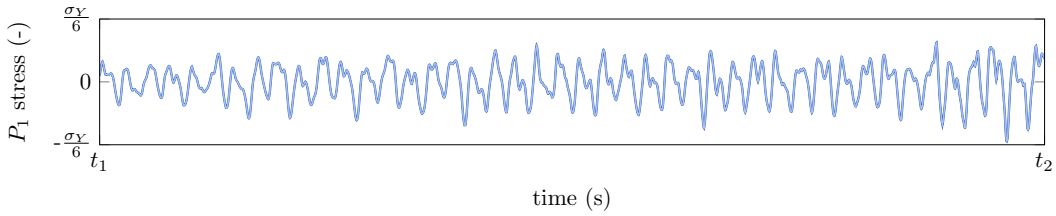

(**b**) time convergence

Figure 7. Time evolution of blade stresses (**a**) with R_s: $R_s = 80$ (——), $R_s = 100$ (——), $R_s = 200$ (——), $R_s = 250$ (——), and (**b**) R_t: $R_t = 1$ (——), $R_t = 500$ (——), $R_t = 1000$ (——), $R_t = 5000$ (——).

The stress field within the full blade finite element mesh at the same time step $t = t_2$ is shown in Figure 8 for different R_s values, and in Figure 9 for different R_t values. The used color code goes from white—no stress—to dark blue—highest stress level, i.e., $\frac{\sigma_Y}{6}$, with σ_Y the yield stress of the blade. Almost identical stress fields are retrieved for all R_s and R_t values. This observation is consistent with the perfect superposition of the stresses time evolution in Figure 7. The dynamical behavior of the blade is therefore identical for all tested R_s and R_t values.

Finally, computation times associated with each simulation are depicted in Figure 10. The horizontal dotted line refers to the simulation time without computing temperatures. All simulations have been performed on a standard computer with an i7-processor. The chosen trade-off between results accuracy and computation times yields 200 thermal abradable coating elements along the circumferential direction (i.e., $R_s = 100$) and $R_t = 1000$. The value of these two parameters is fixed for the following simulations.

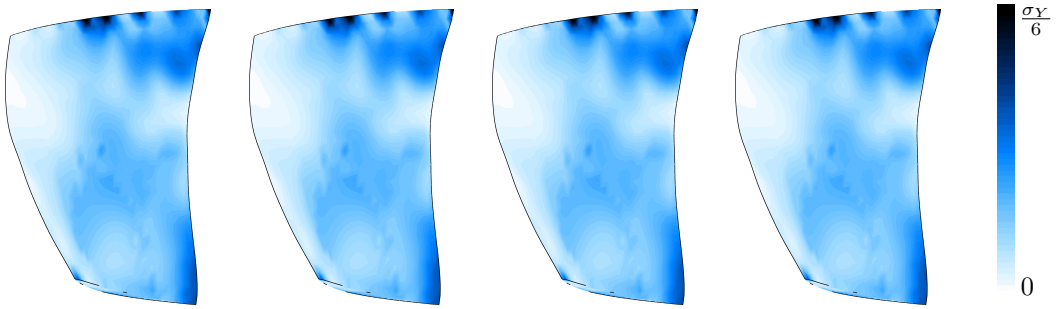

(**a**) $R_s = 80$ (**b**) $R_s = 100$ (**c**) $R_s = 200$ (**d**) $R_s = 250$ (**e**) color code

Figure 8. Blade stress fields for different R_s values.

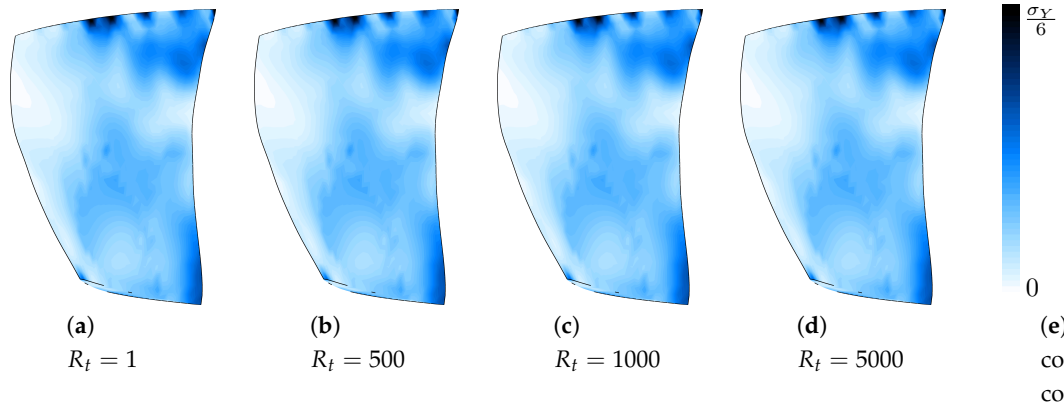

Figure 9. Blade stress fields for different R_t values.

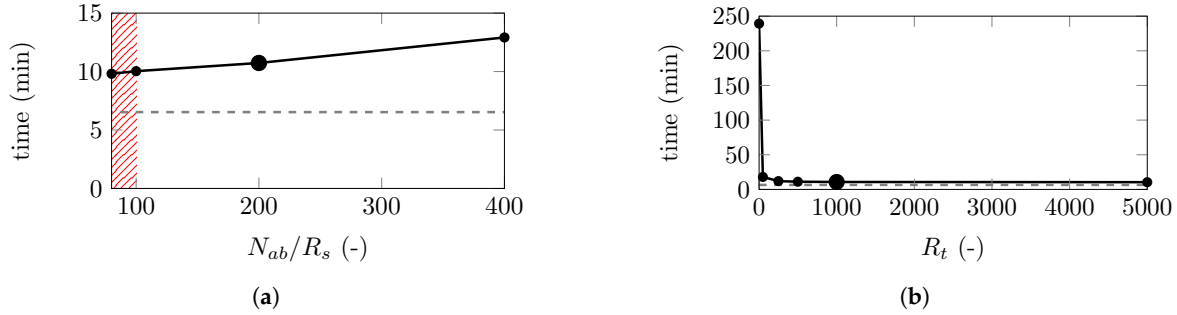

Figure 10. Evolution of the computation time with (**a**) the number of thermal abradable coating elements, and (**b**) with R_t.

4. Experiments

The previously described model is applied here on two experimental data sets: (1) a high-pressure (HP) compressor's bladed disk, and (2) a low-pressure (LP) compressor's bladed disk. Both experimental set-up are first detailed. Then, the temperature field recorded on the first experiment set-up is used to calibrate the numerical thermal model. Finally, the second test is simulated using the calibrated model, and the obtained temperatures are compared with the experiments.

4.1. Calibration of the Thermal Model

The aim of this section is to calibrate the thermal model based on previously published experimental data [3]. The set-up consists of a rotating bladed disk that undergoes contact events with an abradable layer deposited onto a simplified casing. Both the bladed disk and the casing are made of titanium materials, and the abradable layer is made an AlSi alloy. An infrared camera in front of the test set-up recorded temperature increases [3]. The color code ranges from white—no temperature increase—to red—high temperatures. The targeted angular speed is $\Omega_{\text{exp}}^{\text{HP}}$, which corresponds to the 22nd engine order excitation of the first torsion mode, see Figure 4b. 22 hot spots are observed along the casing circumference, and temperatures above 80 °C have been recorded experimentally, as depicted in Figure 11a. A more detailed description of the test set-up and data analyses can be found in [3].

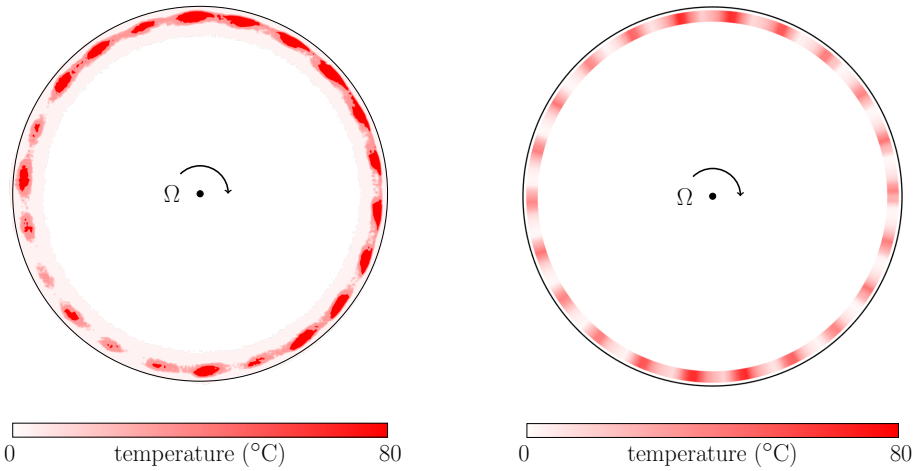

(**a**) experimental [3] (**b**) numerical

Figure 11. Temperature profile for the HP compressor test case.

Simulations are carried out over 100 blade revolutions at constant angular speed corresponding to the experimental value. The values for R_s and R_t parameters are fixed to the values selected in the convergence analysis. The value of the heat flux parameter q_T is calibrated to retrieve the same order of magnitude of temperature increase. The blade displacements at the leading edge (LE), mid-chord (MC) and trailing edge (TE), obtained using the calibrated model, are depicted in Figure 12. The blade displacement exhibits an increasing amplitude (for $t \in [0 - 0.51]$ s) followed by a decreasing amplitude of vibration (for $t > 0.51$ s). Displacements are similar to the ones obtained in [3] without taking into account thermal effects. This similarity in blade displacements is expected because of the low temperature increases during this test (80 °C): the thermal expansion of the abradable layer remains limited and does not significantly affect the blade dynamics.

The corresponding temperature profile at the leading-edge side at $t = 0.51$ s along the abradable layer circumference is plotted in Figure 11b. The 22 high temperature points are retrieved, with the same order of magnitude then the experimental temperature field, i.e., 80 °C (see Figure 11b) which was the calibration point of the thermal model.

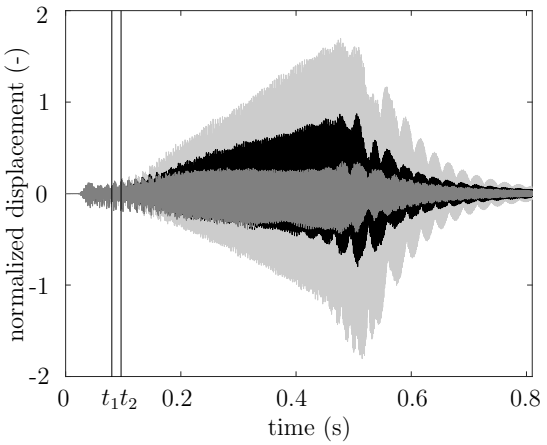

Figure 12. Time evolution of the blade displacement at the leading edge (——), mid-chord (——), and trailing edge (——) for the HP compressor test case.

The obtained wear profile at the leading edge, mid-chord and trailing edge at $t = 0.51$ s is shown in Figure 13. 22-wear lobes are observed at the leading and trailing edges because of the excitation of

the 22-engine order. At mid-chord, 2-wear lobes are obtained, corresponding to the casing deformation applied at the beginning of the simulation to initiate contacts. Because the responding mode is the first blade torsion (1T) mode, the blade has a low amplitude of vibration at mid-chord, and the 22 wear lobes are not visible (see Figure 13b). The temperature profile along the surface of the abradable layer can also be visualized with the red line along the wear profile (therefore, the temperature field in Figure 11b is retrieved in Figure 13a along the wear profile). The high temperature areas—in red in Figure 13a—are localized in front of the 22 wear lobes, as in the experiments, because the heat flux injected within the abradable layer is assumed proportional to the blade/abradable layer friction forces. Moreover, due to heat conduction within the abradable layer from the mid-chord location to the leading and trailing edge sides and to the initial 2-lobe casing deformation, higher temperature levels are achieved in the vicinity of angular positions $\frac{\pi}{2}$ and $\frac{3\pi}{2}$.

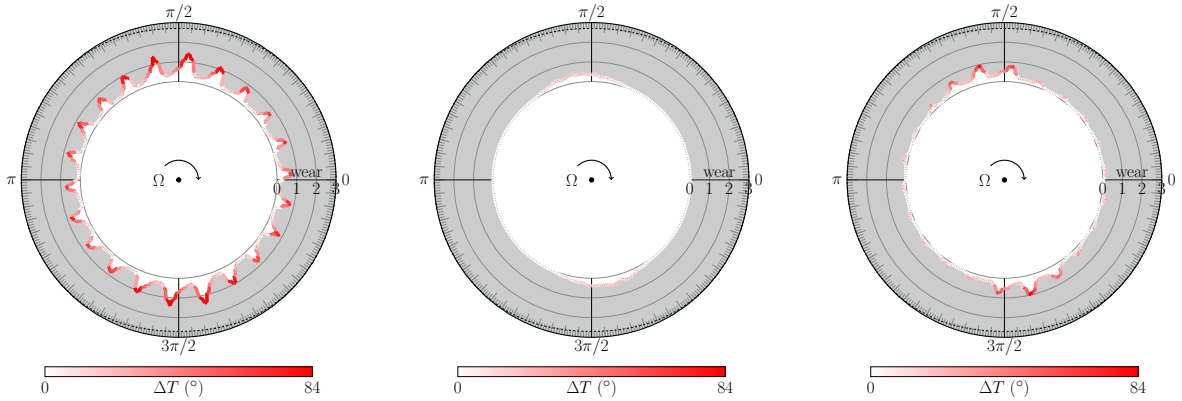

(**a**) LE (**b**) MC (**c**) TE

Figure 13. Wear and temperature profiles at 0.51 s for the HP compressor test case.

The numerical model allows prediction of the blade dynamics and wear profiles, with an order of magnitude for the temperatures which is consistent with experimental data. The calibrated model is therefore assumed relevant and is used in the next section to simulate the second test case.

4.2. Application of the Calibrated Model

The previously calibrated model is used in this section to predict the temperature elevation for the second experimental set-up [2]. This second test is carried out on a single stage of a LP compressor's bladed disk. The finite element model of the LP compressor blade can be seen in Figure 14a. A detailed description of the test and acquired signals can be found in [2]. One blade of the bladed disk is longer than the others to ensure that the contact between the rotor and the casing occurs on this blade. A strain gauge is located on the center of the blade to record its dynamical response. The bladed disk is mounted on a shaft and in a vacuum chamber to avoid aerodynamical loadings and temperature elevation by heat convection. Accelerometers and thermocouples are placed on the external surface of the casing, which is initially ovalized due to assembly conditions. The angular speed is chosen using the Campbell diagram shown in Figure 14b such as the first eigenfrequency—corresponding to the first bending (1B) mode—is excited by the 7th engine order. More precisely, the angular speed is slightly higher than the one corresponding to the intersection of the 1B mode with the 7th engine order due to contact stiffening. During the test, the angular speed is progressively increased to achieve the targeted speed, denoted $\Omega_{\text{exp}}^{\text{LP}}$.

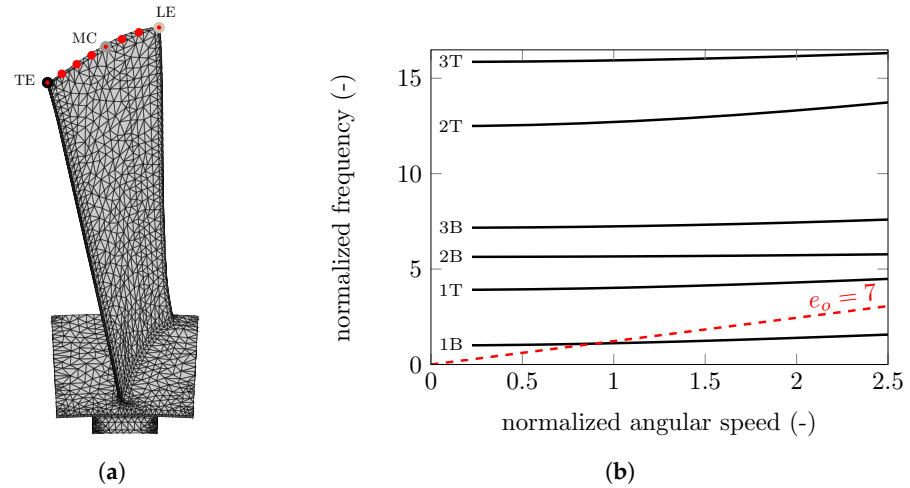

(**a**) (**b**)

Figure 14. Finite element model (**a**) and Campbell diagram (**b**) of the LP compressor blade.

The available data acquired during the experiments are: (1) the time evolution of the blade stresses recorded by the strain gauge, (2) the *post-mortem* wear profile, measured at the end of the experiments, and (3) temperatures on the outer surface of the casing recorded by the temperature probes at eight different angular positions. The detailed analysis of the time evolution of the blade stresses recorded by the strain gauge during the experimental test can be found in [2]. Contrary to the first test case on the HP compressor (see Section 4.1), the time response of the blade displacement always increases with time during the test, leading to a diverging blade motion.

The post-mortem wear profile is measured at the leading edge, mid-chord and leading edge at the end of the experiments using a coordinate measuring machine, every 10° along the circumferential direction. They are pictured in Figure 15. Seven deep wear lobes are observed on the trailing edge's side, with a high wear depth (see Figure 15c). Seven lobes are also observed at mid-chord (see Figure 15b), while almost no wear appears at the leading edge (see Figure 15a). The low wear level at the leading edge is due to the initial ovalization of the casing at the beginning of the test. These differences in the LE, MC and TE wear depths can be explained by the excitation of the 1B mode, which exhibit a large vibration amplitude at the TE and MC and a lower amplitude at the LE. Finally, temperature probes, located on the outer surface of the casing in front of the blade mid-chord at different angular positions, recorded the temperatures during the test. Temperatures measured at the end of the diverging motion are given in Figure 15b. They ranged from +15 to +125 °C. These temperatures seem to be higher at the middle of wear lobes, but data are very sensitive to the angular position. Nevertheless, this allows obtaining of an order of magnitude of the temperature level on the outer surface of the casing. Within the abradable layer, the achieved temperatures will logically be higher than the probe values.

Numerical simulations are conducted to reproduce the test conditions using the calibrated model. The simulation is carried out over 40 blade revolutions at constant angular speed $\Omega_{\text{exp}}^{\text{LP}}$. The space and time discretization parameters, R_s and R_t respectively, are kept the same than the one chosen in Section 3. The convergence of the results for these two parameters has been verified, but the results are not shown here for the sake of brevity. The finite element model of the instrumented blade is shown in Figure 14a. The red dots at the blade tip correspond to nodes retained in the reduced order model. The location of the leading edge (LE), mid-chord (MC), and trailing edge (TE) is also shown.

The obtained time evolution of the blade displacement at the leading edge, mid-chord and trailing edge is shown in Figure 16. As observed in the experiments, amplitude of vibration always increases with time, leading to a divergent interaction. Therefore, stresses within the blade reach the yield stress of the blade material thus leading to crack initiation, in agreement with experimental observations [2]. Also, amplitudes of the blade displacement are higher at the trailing edge and mid-chord, while the

vibration amplitude remains small at the leading edge. The dynamical behavior of the system is therefore well predicted by the numerical model.

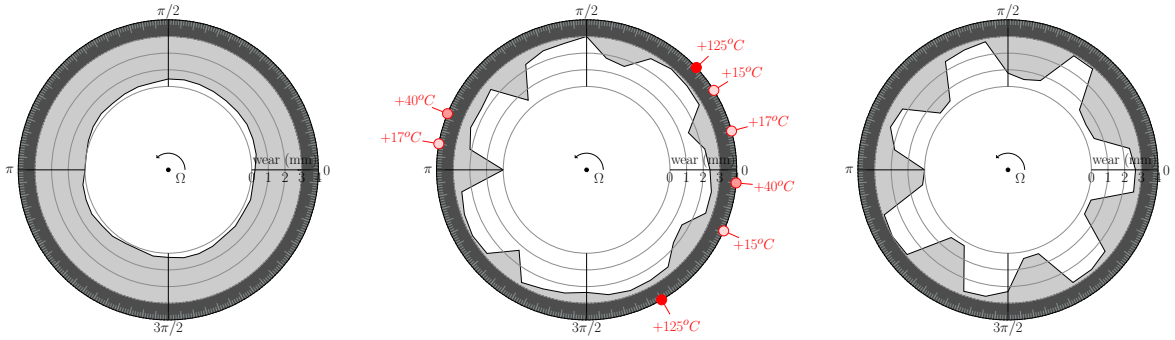

(**a**) LE (**b**) MC (**c**) TE

Figure 15. Experimental wear and temperature profiles for the LP compressor test case [2].

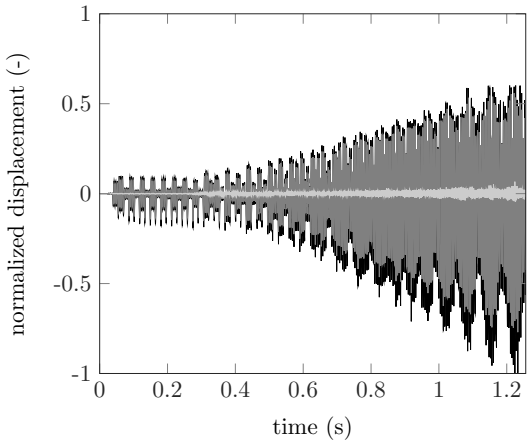

Figure 16. Time evolution of the blade displacement at the leading edge (——), mid-chord (——), and trailing edge (——) for the LP compressor test case.

Figure 17 shows the wear profile at the leading edge, mid-chord and trailing edge at the end of the simulation. These wear profiles obtained numerically can be directly compared with the experimental ones, shown in Figure 15. As in the experiments, seven deep wear lobes are observed at the trailing edge, because of the high blade amplitude of vibration. The abradable layer is removed over all its thickness at the angular positions of the seven wear lobes, and the blade may be in contact with the casing. Seven wear lobes are also observed at mid-chord, and two wear lobes are obtained numerically at the leading edge due to the initial ovalization of the casing. The temperature profile at the end of the simulation is also superimposed along the wear profile in Figure 17. The color code goes from white color—that corresponds to no temperature increase—to red—highest temperature increases. High temperature points are observed in the vicinity of wear lobes. The maximum temperature reached numerically within the abradable layer is 274 °C. This value is higher than the experimental observation (125 °C), but the temperature probes are located on the outer surface of the casing. It seems reasonable to expect higher temperature levels within the abradable layer, considering the heat localization and diffusion time. The order of magnitude of the temperature obtained using the calibrated model to simulate this second experimental test is therefore realistic.

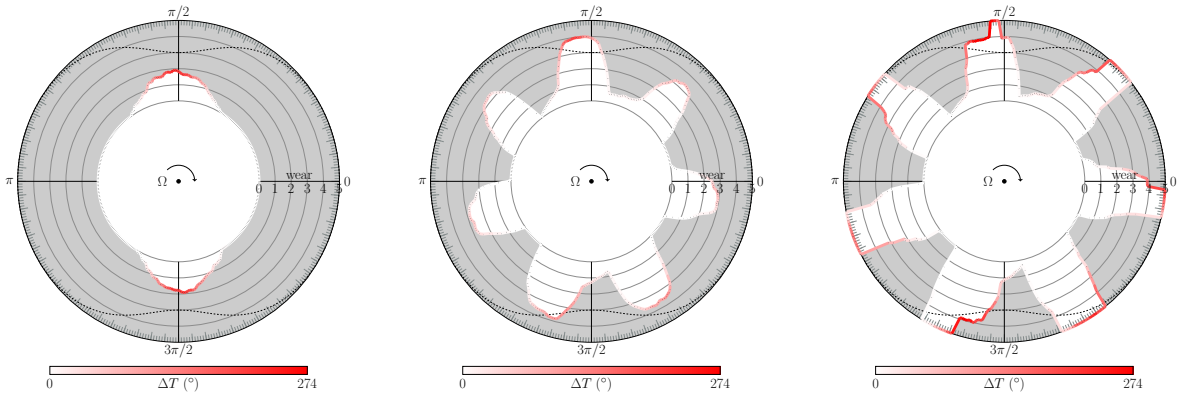

(**a**) LE (**b**) MC (**c**) TE

Figure 17. Numerical wear and temperature profiles for simulations on the LP compressor's blade.

4.3. Partial Conclusion

The numerical model calibrated using the first experimental test case provides realistic temperature values for both experimental test cases. Variations in the abradable coating's material properties or in the probe localization can explain the observed differences between numerical and experimental results. Nevertheless, the order of magnitude of the numerically predicted temperature is coherent with the experiments. Since the thermal flux is modeled as proportional to friction forces—and therefore proportional to the contact forces—the agreement between the temperatures for the two test cases can be directly related to coherent order of magnitudes for numerically predicted contact forces.

Additionally, for both investigated cases, the predicted blade dynamics is similar to experimental observations: (1) for the HP compressor case, a non-diverging interaction on the torsion mode with the 22nd engine order is retrieved, and (2) for the LP compressor blade, a diverging interaction with the first bending mode and the 7th engine order is obtained as in the experiments.

As a conclusion, thanks to the verification of the order of magnitude of contact forces for independent set-ups, the numerical model is assumed predictive in different configurations. Therefore, further detailed investigations on the system dynamical behavior and on the resulting rotor/stator interactions can be performed with confidence in the numerical predictions.

5. Sensitivity Analysis

In this section, a detailed sensitivity analysis of the observed interactions is carried out for both the HP and LP compressor blades. More particularly, the effect of the angular speed and the initial clearance between the blade and the abradable layer is investigated. Indeed, previous work showed that a precise modeling of the blade/casing clearances is key to accurately predict contact interaction phenomena [16]. Due to intrinsic nonlinearity of the system, a small change in the engine working conditions may lead to completely different amplitudes of vibration and dynamical behavior.

5.1. High-Pressure Compressor Blade

A sensitivity analysis in terms of the angular speed and the initial clearance is performed here on the HP compressor blade shown in Figure 4a. The calibrated model is used for all simulations. First, the influence of the angular speed is studied on its own. Indeed, due to contact stiffening and to the intrinsic nonlinear nature of the studied phenomena, the angular speed at which interactions may occur is difficult to predict *a priori*. The dynamical response of the system is very sensitive to the angular speed. Simulations are therefore carried out over a range of angular speeds in the vicinity of the targeted interaction speed. Then, the same analysis is performed with a variation of the initial clearance since this parameter is key for contact interaction initiation. Finally, their coupled influence is analyzed.

5.1.1. Influence of the Angular Speed

Simulations are performed over a wide range of angular speeds around the experimental angular speed, denoted Ω_{exp}^{HP}. Each simulation is carried out at constant angular speed over 100 blade revolutions.

The evolution of the wear profile for different angular speeds at both leading and trailing edges along the circumference of the abradable coating taking into account thermal effects is shown in Figure 18. Dark areas refer to high wear levels while white color correspond to no wear. Depending on the angular speed, different interactions are observed: 9-wear lobes are identified with a high wear level around 0.95 Ω_{exp}^{HP} (excitation frequency corresponding to crossing between 9th engine order and the first blade bending mode, see Figure 4b), 22-wear lobes around Ω_{exp}^{HP} (crossing between 22nd engine order and the first blade torsion mode in Figure 4b), and 8-wear lobes around 1.05 Ω_{exp}^{HP} (crossing between 8th engine order and the first blade bending mode, see Figure 4b). Between these interaction areas, the observed 2-wear areas at angular positions $\frac{\pi}{2}$ and $\frac{3\pi}{2}$ are due to the initial casing deformation. Figure 19 shows the temperature profiles for different angular speeds at both leading and trailing edges along the circumference of the abradable coating. High temperature areas are observed in the vicinity of wear lobes because of the definition of the heat flux which is proportional to the blade/abradable layer friction forces. The two observed bending interactions (with engine orders 9 and 8) respond over a large angular speed range. The wear depth and the temperature increase are also higher, with all the abradable layer removed and localized high temperature points. When starting the engine, the angular speed progressively increases up to the nominal value. This wide interaction area will therefore be crossed. The torsion interaction occurs for a limited angular speed range. The wear depth is also lower than for the bending interaction, and the temperature is more uniform along the casing circumference.

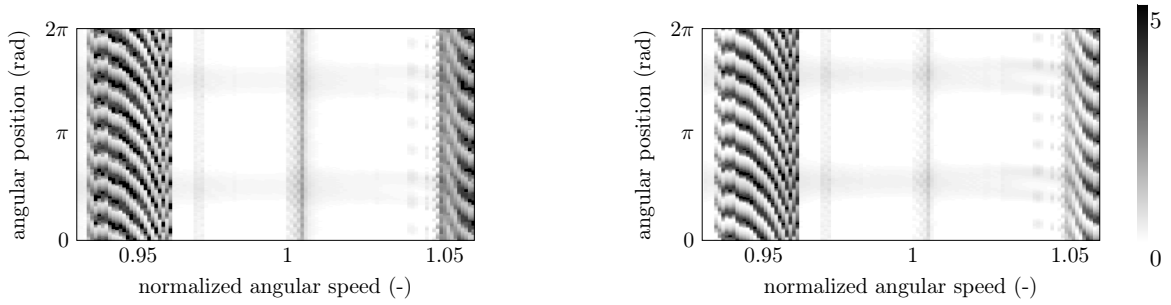

(**a**) LE (**b**) TE

Figure 18. Evolution of the wear profile with the angular speed for the HP compressor blade.

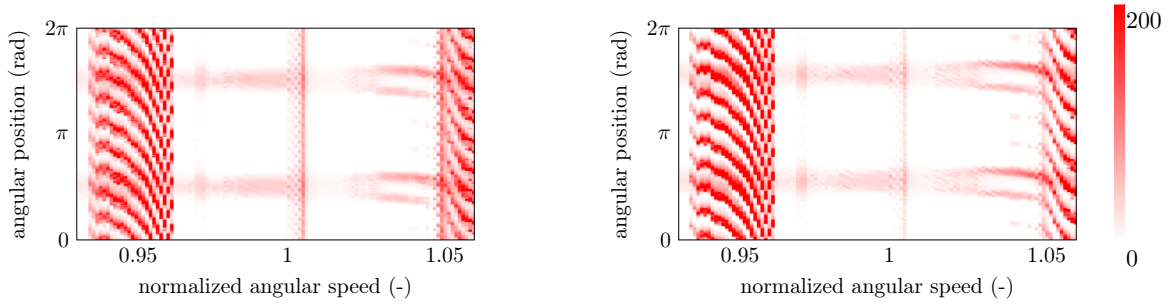

(**a**) LE (**b**) TE

Figure 19. Evolution of the temperature profile with the angular speed for the HP compressor blade.

A succession of blade/casing interactions are observed as the angular speed increases, with both bending and torsion modes. Abrupt changes of dynamical behavior are observed, with higher

wear depth for bending interactions. The angular position $\frac{\pi}{2}$ and $\frac{3\pi}{2}$ are privileged areas for high temperatures.

5.1.2. Influence of the Initial Clearance

Various research has been conducted to quantify the effect of the clearance between the tip of the blades and the casing from the aerodynamical point of view because of its high influence on the engine performance [17–20]. In this section, a sensitivity analysis to the clearance between the blade and the abradable coating is carried out in terms of structural dynamics and rotor/stator interaction.

The evolution of the frequency response function of the blade displacement at constant angular speed, equal to $\Omega_{\text{exp}}^{\text{HP}}$, for an increasing initial clearance is shown in Figure 20. Three distinct areas can be identified, for which different modes respond. Area 1 corresponds to an interaction with the first bending mode. Area 2 is related to the 22-lobe interaction with the torsion mode. In area 3, for which the initial gap is larger (>0.38), the bending mode is again excited but with lower amplitude and a different engine order. The abrupt changes observed between the different areas, especially between areas 2 and 3, are due to the nonlinear intrinsic characteristic of contact interactions. The differences in the initial conditions lead to a system response along different modes.

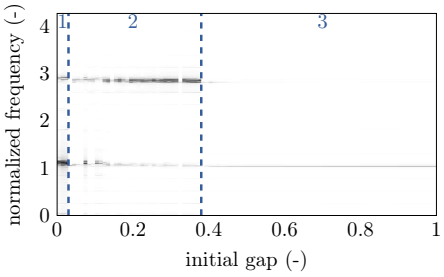

Figure 20. Evolution of the frequency response function of the blade displacement with the initial clearance for the HP compressor blade.

The evolution of the wear profile at the leading and trailing edge with the initial clearance is shown in Figure 21, and the corresponding evolution of the space Fourier transform of the wear profile is depicted in Figure 22. The same three areas can be distinguished. In area 1, 17-wear lobes are observed at both leading and trailing edges, with a high wear level. Wear level is slightly higher at the leading edge than the trailing edge. In area 2, 22-wear lobes can be identified. This corresponds to the 22-lobe interaction experimentally observed (see Section 4.1). This interaction is obtained over a large range of initial clearance ($[0.05 - 0.38]$). In area 3, which corresponds to larger initial gaps, even harmonics and 2 wear lobes are obtained. These 2-wear lobes are due to the initial deformation of the casing (see Figure 1), and no interaction occurs for high clearance values. The wear level is also lower in the area.

The associated temperature maps are shown in Figure 23. As expected, the three areas can also be observed, with respectively 17, 22 and 2 high temperature spots. However, in the second area, two high temperature areas can be additionally shown. This is because the first torsion mode is mainly excited, and at the middle of the blade, only two contact areas are observed (related to the 2-wear-lobe initial casing deformation) instead of 22. The diffusion within the abradable coating in these two areas leads to higher temperatures.

These results suggest that a clearance reduction may lead to unexpected effects on the engine dynamics in terms of rotor/stator interactions. On the contrary, a small increase of the initial clearance completely eliminates the interaction of interest, which would be beneficial for the engine blade dynamics if this gap increase does not affect the overall aerodynamic performance. Moreover, the clearance reduction does not have the same effect than an angular speed increase. Even if these two variations of configuration both lead to a blade-tip/abradable layer distance

reduction—centrifugal loadings are taken into account in the model—the 17-wear lobes interaction is initiated only at low clearance values.

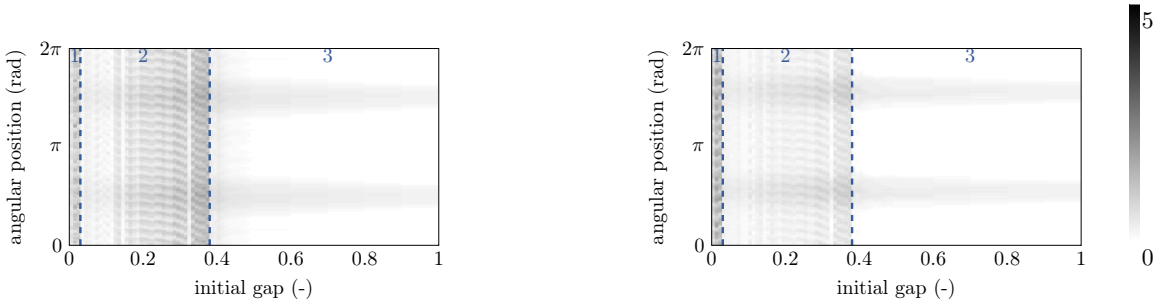

(**a**) LE (**b**) TE

Figure 21. Evolution of the wear profile with the initial clearance for the HP compressor blade.

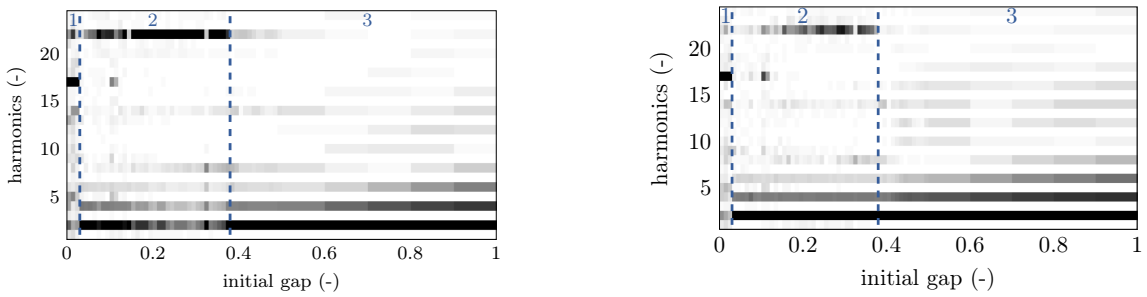

(**a**) LE (**b**) TE

Figure 22. Evolution of the space Fourier transform of the wear profile with the initial clearance for the HP compressor blade.

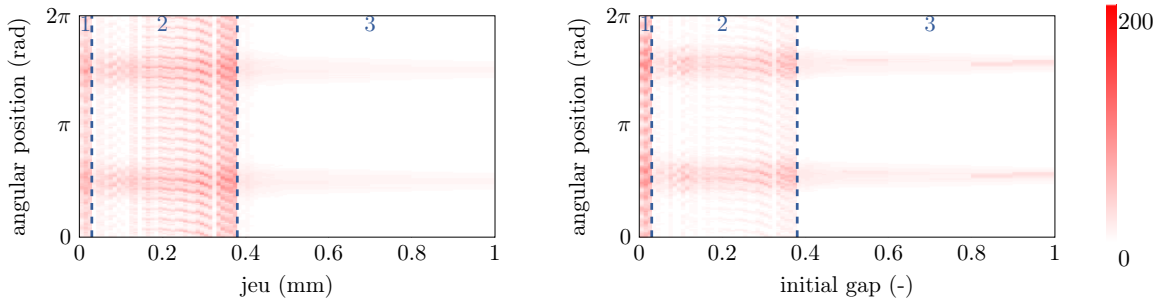

(**a**) LE (**b**) TE

Figure 23. Evolution of the temperature profile with the initial clearance for the HP compressor blade.

5.1.3. Cross Analysis

Depending on the angular speed and the initial clearance, different interactions have been observed. A coupled influence of both parameters is carried out in this section. In particular, Figure 24 summarizes the number of wear lobes obtained depending on the angular speed and the initial clearance. The angular speed axis is normalized using the experimental value as reference. Three different interactions are observed: 5 wear lobes (■) at higher angular speed for low initial gap values, 17 wear lobes (■) at low initial gap values, and 22 wear lobes (■) for intermediate gap values.

The experimentally observed 22-wear-lobe interaction occurs for smaller initial clearance values as the angular speed increases. This can be explained by the centrifugal loading that increases with the

angular speed. Indeed, the effective gap between the blade and the casing is equal to the initial gap reduced by the centrifugal displacement of the blade at the considered angular speed. For the smallest values of the initial gap, a 17-wear-lobe interaction appears but it is initiated for some distinct gap values. The initiation of this interaction is therefore very sensitive to initial conditions. For angular speeds above 1.1 Ω_{exp}^{HP}, the clearance reduction leads to 5 wear lobes. For high initial clearance values, no interaction is observed for any angular speed. Therefore, the effect of the initial clearance leads to a more complex dynamics than the angular speed variation.

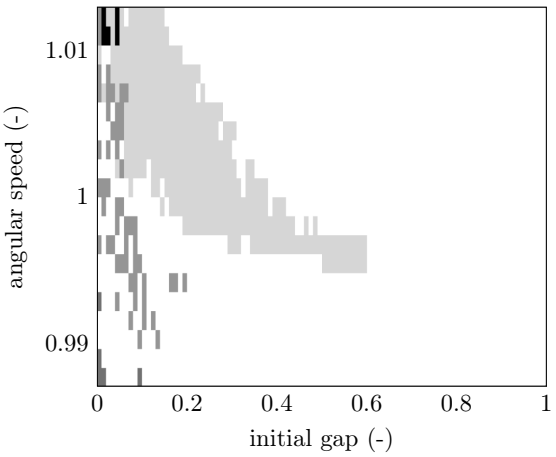

Figure 24. Number of wear lobes depending on the angular speed and the initial clearance for the HP compressor blade. (■): 5 wear lobes, (■): 17 wear lobes, (■): 22 wear lobes.

5.2. Low-Pressure Compressor Blade

The same three analyses are performed for the LP compressor blade in this section: the influence of the angular speed, of the initial clearance, and the coupled influence on the observed interactions.

5.2.1. Influence of the Angular Speed

The wear maps obtained over a range of angular speeds centered around the experimental angular speed (considered to be reference) at the LE and TE are shown in Figure 25, and the corresponding temperature maps are given in Figure 26. Abrupt changes in the blade behavior are observed. For the considered angular speed range, two interaction areas—with 8 and 7 wear lobes—are observed, both at the blade trailing edge only. These two interactions are due to the crossing between the first bending frequency with the different engine order curves. As for the HP compressor case, deeper wear lobes are observed for bending interactions. All the abradable layer is removed in front of lobes angular position. This means that higher blade amplitudes of vibrations are generated for these interactions. Between these two strong interaction areas, different numbers of lobes are observed: 4 lobes in the angular speed range $[0.9 - 1]\ \Omega_{exp}^{LP}$, 6 lobes for $\Omega > 1.05\ \Omega_{exp}^{LP}$, and an interaction with 13 wear lobes is also locally observed at the angular speed $\Omega = 1.1\ \Omega_{exp}^{LP}$.

High temperature points are observed in Figure 26 at high wear angular positions, especially for the interaction with the 8th and 7th engine orders. Indeed, deeper wear lobes are related to higher friction forces, and higher heat flux. In the angular speed range $[0.9 - 1]\ \Omega_{exp}^{LP}$, two high temperature areas are observed due to the casing ovalization. Heat conduction from the leading edge to the trailing edge exacerbates the two high temperature strips. For $\Omega > 1.05\ \Omega_{exp}^{LP}$, 4 high temperature bands are shown at angular positions $\frac{\pi}{2}$ and $\frac{3\pi}{2}$ again because of the high contribution of heat from the leading edge's side. For the same reason, the wear lobes at angular positions 0 and π leads to lower temperature levels because no contribution from the leading edge. At the angular speed $\Omega = 1.1\ \Omega_{exp}^{LP}$, 13 high temperature points are observed at the position of the wear lobes.

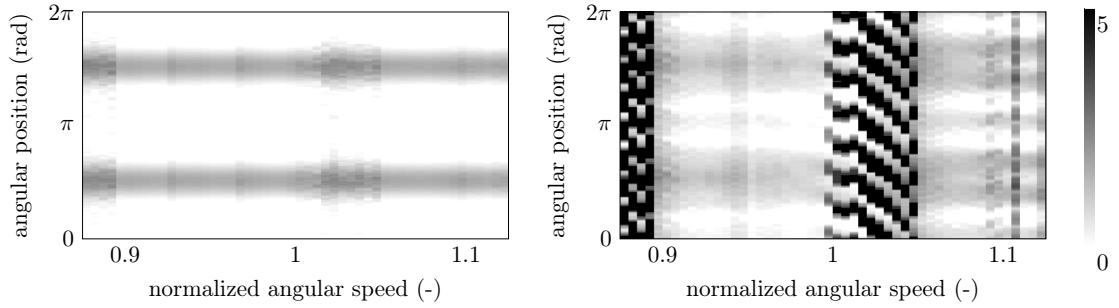

(**a**) LE (**b**) TE

Figure 25. Evolution of the wear profile with the angular speed for the LP compressor blade.

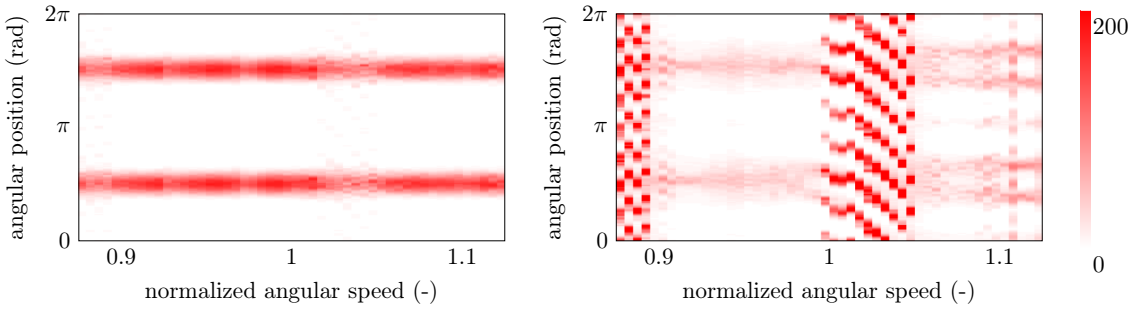

(**a**) LE (**b**) TE

Figure 26. Evolution of the temperature profile with the angular speed for the LP compressor blade.

5.2.2. Influence of the Initial Clearance

As for the HP compressor's blade, the influence of the initial clearance on the observed interaction is detailed. Higher gap values are studied since LP compressor blade are taller than blades within a HP compressor and have higher centrifugal displacements. Figure 27 show the evolution of the wear profile along the casing circumference while increasing the initial gap between the blade and the casing. The space Fourier transform of the wear maps with respect to the initial clearance is depicted in Figure 28. The evolution of the temperature profiles along the casing circumference with the initial gap is shown in Figure 29. On these graphs, three distinct areas can be identified. For low values of the initial gap, an unclear 7-wear lobes interaction is observed. When increasing the initial clearance, 7 deep wear lobes are obtained on the wear map at intermediate values. Finally, at higher values of the initial clearance, an abrupt change of behavior occurs, and no more interaction is observed. The 2 wear lobes correspond to the initial deformation of the casing. For all values, the interaction remains localized on the trailing edge only. The structure responds along its first bending mode, which exhibits a larger amplitude of vibration at the trailing edge. Contrary to the HP compressor case, deeper wear lobes are observed in area 2, while area 1 does not exhibits strong interactions. Therefore, reducing the initial clearances does not generate here unexpected and potentially damaging rotor/stator interactions. In Figure 29, high temperature points follow the wear profiles with a dominance (especially at low initial clearance) in the 2-wear-lobe areas because of the heat conduction within the blade. Because the wear depth is significant in area 2 at trailing edge, the heat transfer from the leading to the trailing edge is less pronounced than for the two other areas.

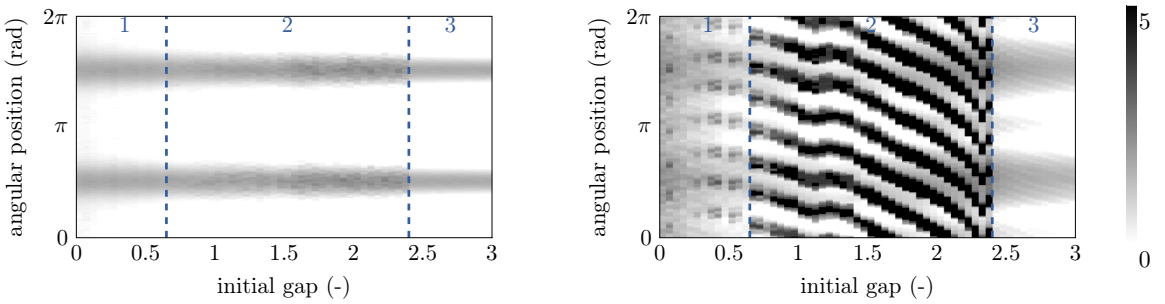

(**a**) LE (**b**) TE

Figure 27. Evolution of the wear profile with the initial clearance for the LP compressor blade.

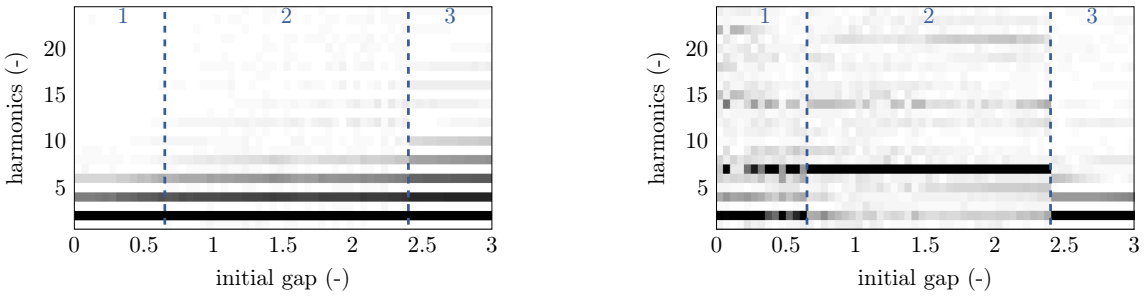

(**a**) LE (**b**) TE

Figure 28. Evolution of the space Fourier transform of the wear profile with the initial clearance for the LP compressor blade.

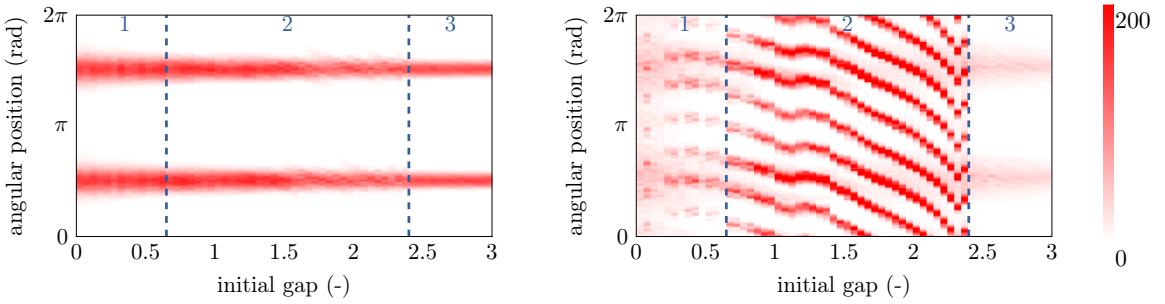

(**a**) LE (**b**) TE

Figure 29. Evolution of the temperature profile with the initial clearance for the LP compressor blade.

5.2.3. Cross Analysis

The interactions observed with respect to the initial blade-tip clearance and the angular speed are summarized in Figure 30. The angular speed axis is normalized using the experimental value as reference. Two different interactions are observed when varying the initial clearance and angular speed: 7 wear lobes (■), and 15 wear lobes (■). As for the HP compressor blade, the higher the angular speed, the lower initial clearance interactions occur. However, the two interaction areas are here well separated, with a more stable initiation of the interaction with the initial conditions. The 15 wear lobes is observed only at lower angular speed while the 7th engine order interaction responds for a large range of angular speeds and initial clearances. This cross analysis shows that depending on the engine nominal angular speed, a reduction of the nominal clearances in the engine design in order to improve the aerodynamic performance can lead to a risk of occurrence of interactions with other engine orders.

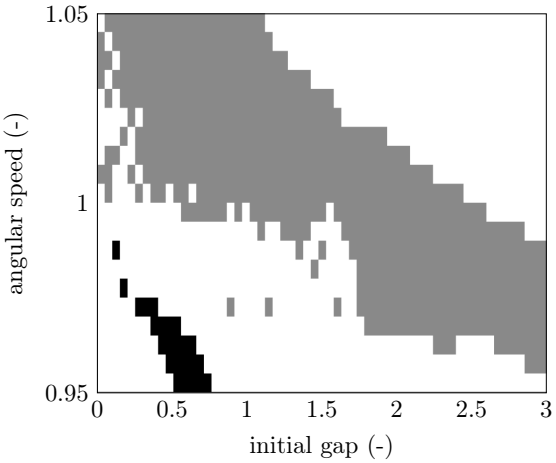

Figure 30. Number of wear lobes depending on the angular speed and the initial clearance for the LP compressor blade. (▪): 7 wear lobes, (▪): 15 wear lobes.

6. Conclusions

This paper uses a numerical model taking into account thermal effects in the abradable coating to validate contact forces prediction through the comparison of two experimental set-up. The numerical modeling of the abradable layer consists of (1) a mechanical mesh made of independent two-node rod elements with elasto-plastic constitutive law to compute the abradable wear, and (2) a thermal mesh added to compute the evolution of the temperature in the abradable layer following blade contacts. The blade heat flux is assumed to be proportional to the friction forces between the blade and the abradable coating. A dependence of the mechanical properties of the abradable coating with temperature is also included. To reduce computation times, distinct space and time discretizations are used to solve the thermal and mechanical problems. A convergence analysis is performed, which shows that the space and time discretization has low effects on the obtained wear and temperature profiles as well as for the blade response.

A calibration of the blade heat flux has been carried out using experimental data acquired on a high-pressure compressor blade. The aim of the calibration was to retrieve the same temperature increases as observed in the experiments. This calibrated value has been kept to predict temperature levels for another set of experimental data, obtained from a low-pressure compressor blade. Because of the definition of the heat flux, proportional to the friction forces, the fact that realistic temperatures are obtained for two independent test cases with two distinct structures gives confidence in the numerically predicted contact forces.

Based on this calibrated model, further analyses in terms of the effect of the initial clearances—which is a key parameter in the initiation of contact interactions—and of the rotor angular speeds have been carried out. Both low-pressure and high-pressure compressor test cases have been investigated. A coupled influence of the angular speed and the initial clearance has also been conducted. It has been found that interactions occur for smaller initial clearance values as the angular speed increases. This is explained by the centrifugal load of the blade. But when decreasing the initial clearance at a given angular speed, unexpected interactions may appear, which were observed for the studied high-pressure compressor blade in particular. Different interactions for low gap values appear for this blade. However, for the low-pressure compressor blade, the studied interactions were more robust. Reducing the initial clearances is a common solution to improve aerodynamical engine performance. However, a detailed analysis of this clearance reduction is recommended since it may lead, for some blades, to detrimental dynamical behavior.

Author Contributions: Conceptualization, F.N. and A.B.; methodology, F.N.; validation, F.N.; formal analysis, F.N.; investigation, F.N.; writing—original draft preparation, F.N.; writing—review and editing, F.N. and A.B.; supervision, A.B.; project administration, A.B.; funding acquisition, A.B. All authors have read and agreed to the published version of the manuscript.

Funding: This research was supported by the Fonds de Recherche du Quebec—Nature et Technologies (FRQNT) and the Natural Sciences and Engineering Research Council of Canada (NSERC).

Conflicts of Interest: The authors declare no conflict of interest. The funders had no role in the design of the study; in the collection, analyses, or interpretation of data; in the writing of the manuscript, or in the decision to publish the results.

References

1. Williams, R.J. Simulation of blade casing interaction phenomena in gas turbines resulting from heavy tip rubs using an implicit time marching method. In Proceedings of the ASME Turbo Expo 2011 Conference, GT2011-45495, Vancouver, BC, Canada, 6–11 June 2011.
2. Millecamps, A.; Brunel, J.; Dufrénoy, P.; Garcin, F.; Nucci, M. Influence of thermal effects during blade-casing contact experiments. In Proceedings of the ASME 2009 IDETC & CIE Conference, ASME, San Diego, CA, USA, 30 August–2 September 2009.
3. Batailly, A.; Agrapart, Q.; Millecamps, A.; Brunel, J.F. Experimental and numerical simulation of a rotor/stator interaction event within an industrial high-pressure compressor. *J. Sound Vib.* **2016**, *375*, 308–331. [CrossRef]
4. Muszynska, A.; Bently, D.; Franklin, W.; Hayashida, R.; Kingsley, L.; Curry, A. *Influence of Rubbing on Rotor Dynamics—Part 1*; Technical Report NAS8-36179; NASA: Washington, DC, USA, 1989.
5. Borel, M.; Nicoll, A.; Schlapfer, H.; Schmid, R. The wear mechanisms occurring in abradable seals of gas turbines. *Surf. Coat. Technol.* **1989**, *39*, 117–126. [CrossRef]
6. Mandard, R.; Witz, J.F.; Boidin, X.; Fabis, J.; Desplanques, Y.; Meriaux, J. Interacting force estimation during blade/seal rubs. *Tribol. Int.* **2015**, *82*, 504–513. [CrossRef]
7. Salles, L.; Blanc, L.; Thouverez, F.; Gouskov, A. Dynamic analysis of fretting wear in friction contact interfaces. *Int. J. Solids Struct.* **2010**, *48*, 1513–1524. [CrossRef]
8. Baïz, S. Etude expérimentale du contact aube/abradable: contribution à la caractérisation mécanique des matériaux abradables et de leur interaction dynamique sur banc rotatif avec une aube. Ph.D. Thesis, Ecole Centrale de Lille, Villeneuve-d'Ascq, France, 2011.
9. Legrand, M.; Batailly, A.; Pierre, C. Numerical investigation of abradable coating removal through plastic constitutive law in aircraft engine. *J. Comput. Nonlinear Dyn.* **2011**, *7*, 011010. [CrossRef]
10. Nyssen, F.; Batailly, A. Thermo-Mechanical Modeling of Abradable Coating Wear in Aircraft Engines. *J. Eng. Gas Turbines Power* **2019**, *141*, 021031. [CrossRef]
11. Sternchüss, A.; Balmès, E. On the reduction of quasi-cyclic disks with variable rotation speeds. In Proceedings of the International Conference on Advanced Acoustics and Vibration Engineering (ISMA), Leuven, Belgium, 18–20 September 2006; pp. 3925–3939.
12. Palfrey-Sneddon, H.; Neely, A.J.; Smith, E.O. The influence of descent and taxi profiles on the thermal state of a jet engine at shutdown. In Proceedings of the ISABE 2017 Conference, Manchester, UK, 3–8 September 2017.
13. Adam, L. Modélisation du comportement thermo-élasto-viscoplastique des métaux soumis à grandes déformations. Application au formage superplastique. Ph.D. Thesis, Université de Liège, Liège, Belgium, 2003.
14. Debard, Y. *Méthode des éléments finis: thermique*; Université du Mans: Le Mans, France, 2011.
15. Jeong, C.Y. Effect of Alloying Elements on High TemperatureMechanical Properties for Piston Alloy. *Mater. Trans.* **2012**, *53*, 234–239. [CrossRef]
16. Batailly, A.; Legrand, M.; Millecamps, A.; Garcin, F. Conjectural bifurcation analysis of the contact-induced vibratory response of an aircraft engine blade. *J. Sound Vib.* **2015**, *348*, 239–262. [CrossRef]
17. Layachi, M.Y.; Bölcs, A. Effect of the axial spacing between rotor and stator with regard to the indexing in an axial compressor. In Proceedings of the ASME Turbo Expo 2001 Conference, GT2017-64342, New Orleans, LA, USA, 4–8 June 2001.

18. Ameli, A. Numerical simulation of rotor/stator interaction and tip clearance flow in centrifugal compressors. Master's Thesis, Lappeenranta University of Technology, Lappeenranta, Finland, 2015.
19. Gourdain, N.; Wiassow, F.; Ottavy, X. Effect of Tip Clearance Dimensions and Control of Unsteady Flows in a Multi-Stage High-Pressure Compressor. *J. Turbomach.* **2012**, *134*, 051005. [CrossRef]
20. Feng, J.; Luo, X.; Guo, P.; Wu, G. Influence of tip clearance on pressure fluctuations in an axial flow pump. *J. Mech. Sci. Technol.* **2016**, *30*, 1603–1610. [CrossRef]